PHOTONICS Research

Mid-infrared broadband optical frequency comb generated in MgF_2 resonators

Wei Wu,[1,2] Qibing Sun,[1,2,*] Yi Wang,[1,2] Yu Yang,[3] Xianshun Ming,[1] Lei Shi,[1,2] Keyi Wang,[3] Wei Zhao,[1,2] and Leiran Wang[1,2,4]

[1]State Key Laboratory of Transient Optics and Photonics, Xi'an Institute of Optics and Precision Mechanics, Chinese Academy of Sciences, Xi'an 710119, China
[2]University of Chinese Academy of Sciences, Beijing 100049, China
[3]Department of Precision Machinery and Precision Instrumentation, University of Science and Technology of China, Hefei 230026, China
[4]e-mail: lionking@opt.ac.cn
*Corresponding author: qbsun@opt.ac.cn

Received 25 March 2022; revised 2 June 2022; accepted 21 June 2022; posted 22 June 2022 (Doc. ID 459478); published 27 July 2022

Microresonator-based optical frequency combs are broadband light sources consisting of equally spaced and coherent narrow lines, which are extremely promising for applications in molecular spectroscopy and sensing in the mid-infrared (MIR) spectral region. There are still great challenges in exploring how to improve materials for microresonator fabrication, extend spectral bandwidth of parametric combs, and realize fully stabilized soliton MIR frequency combs. Here, we present an effective scheme for broadband MIR optical frequency comb generation in a MgF_2 crystalline microresonator pumped by the quantum cascade laser. The spectral evolution dynamics of the MIR Kerr frequency comb is numerically investigated, revealing the formation mechanism of the microresonator soliton comb via scanning the pump-resonance detuning. We also experimentally implement the modulation instability state MIR frequency comb generation in MgF_2 resonators covering from 3380 nm to 7760 nm. This work proceeds microresonator-based comb technology toward a miniaturization MIR spectroscopic device that provides potential opportunities in many fields such as fundamental physics and metrology.

https://doi.org/10.1364/PRJ.459478

1. INTRODUCTION

Optical frequency combs (OFCs) have been attracting significant interest over the last two decades as excellent broadband coherent light sources, revolutionizing optical frequency metrology and spectroscopy [1–4]. Investigations of OFCs in a wide range of wavelengths from visible to mid-infrared (MIR) have been reported [5,6]. The MIR spectral region (~2–20 μm) has been a hot topic of ongoing research for the following reasons. On the one hand, this wavelength range is known as the "molecular fingerprint" region and allows for direct exploration of the fundamental absorption bands of many gas molecules, where the absorption strengths of molecular transitions are typically 1 to 2 orders of magnitude higher than those in the near-infrared region [7,8]. On the other hand, it contains two important atmospheric transmission windows, i.e., 3–5 μm and 8–13 μm, that are related to free space communication and environmental monitoring [9]. Thus, MIR laser spectroscopy has numerous applications in biomedicine, defense, environment monitoring, and sensing [10,11]. MIR OFCs offer an attractive way for identifying and quantifying molecular species in a given environment [6,12]. Compared with previous MIR OFCs based on solid-state lasers, semiconductor lasers, and fiber lasers, microresonator-based combs that are free of bulky and complicated components are ideal light sources in practical applications [13–15].

Recently, there have been several demonstrations of MIR frequency comb generation based on microresonators, for example, silicon nitride (Si_3N_4) [16], silicon (Si) [17], crystalline calcium fluoride (CaF_2) [18], and magnesium fluoride (MgF_2) microresonators [19]. However, those microresonator-based MIR frequency combs based on Si_3N_4 and Si platforms are difficult to extend beyond 5 μm because of the limitation of material property. It should be noted that fluoride crystalline resonators have not only ultra-high Q factor in the broad transparent wavelength range from ~0.1 μm to ~10 μm [20] but also naturally anomalous material dispersion that can be further adjusted with resonator geometry [19]. In addition, with narrow linewidth, high output power, and broad spectral coverage, the quantum cascade laser (QCL) has attracted increasing attention as an excellent MIR laser source [21,22]. Therefore, a highly promising route to the broadband MIR frequency comb generation is pumping MgF_2 crystalline microresonators by a

QCL, and this will lead to the access of longer wavelengths in the MIR region.

In this paper, we demonstrate a microresonator-based broadband Kerr frequency comb centered at about 4.78 μm pumped by the QCL. The simulation results show that the intracavity power exhibits characteristic step-like patterns via scanning the frequency of the pump laser from the blue to red detuning, and the microcombs will undergo the modulation instability (MI), multi-soliton, and steady single-soliton states in this process. The temporal and spectral evolution dynamics of single soliton formation in the MgF_2 resonator are also analyzed in detail. The MI state OFC over an ultra-wide bandwidth of 4380 nm generated in the MgF_2 microresonator is experimentally realized by adjusting the pump power and pump-resonance detuning in the MIR region. These results provide a path toward a portable and compact broadband MIR comb source via combining crystalline microresonators with miniaturized QCLs and can offer exciting opportunities for molecular spectroscopy, frequency metrology, and trace-gas detection.

2. DEVICE DESIGN

The MgF_2 crystalline resonator with exceptional optical, mechanical, and chemical properties is chosen for MIR frequency comb generation. The unique combination of MgF_2 material properties includes an excellent mechanical stability, small thermo-refractive constant, and ultra-wide transparency window from the ultraviolet to the MIR. Moreover, the anomalous group velocity dispersion (GVD) over the full MIR region of this material is particularly relevant for achieving the high efficiency broadband four-wave mixing (FWM) process. The MgF_2 resonator is fabricated by using the ultra-precision machining technology [23], and a side-view optical micrograph is exhibited in Fig. 1(a). Diameters of resonators typically range from 0.5 mm to 10 mm, corresponding to the free spectral range (FSR) varying from 7 GHz to 140 GHz. Figure 1(b) presents the calculated intensity profile of the fundamental mode of the MgF_2 microresonator at 4.78 μm. Using the mode solver based on the finite element method (COMSOL Multiphysics), an effective mode area $A_{\text{eff}} \sim 120\ \mu\text{m}^2$ and a nonlinearity coefficient $\gamma = 2\pi n_2/(\lambda A_{\text{eff}}) = 1 \times 10^{-4}\ \text{m}^{-1}\,\text{W}^{-1}$ are obtained in a MgF_2 resonator with a diameter of 2 mm and wedge angle of 30°, where $n_2 \sim 0.92 \times 10^{-20}\ \text{m}^2\,\text{W}^{-1}$ is the nonlinear Kerr coefficient of MgF_2. Limited by the tuning rate and step size of MIR QCL lasers, the quality factor (Q factor) of the microresonators cannot be directly measured in the MIR band. An alternative way is to utilize the NIR data to estimate the Q factor of the MIR band, so the transmission spectrum of the MgF_2 resonator is measured via a tunable narrow-linewidth laser (Toptica CTL 1550) at the communication band with a scanning rate of 0.2 nm/s, as illustrated in Fig. 1(c). By Lorentzian fitting of a resonance mode centered at 1555.038 nm, we measure the typical full width at half-maximum to be 0.88 MHz, giving a loaded Q factor of 2.2×10^8. The Q factor at 4.78 μm is reduced by about an order of magnitude due to the multiphoton absorption of the MgF_2 crystalline microresonator at the MIR region [20,24]. To couple evanescently QCL light into the resonator, a tapered optical fiber made of chalcogenide (ChG) glass is employed because ChG is the superior material due to its broadband transparency and low loss in the MIR [25,26]. The uncoated ChG (As_2S_3) tapered fibers are fabricated with high precision via an electrically heated taper-drawing process [27]. The taper waist diameter can be precisely controlled to phase match the fundamental mode of the resonator by feedback control of the tapering setup, and Fig. 1(d) shows the suitable taper waist diameter of approximately 1.5 μm for light coupling to a MgF_2 microresonator.

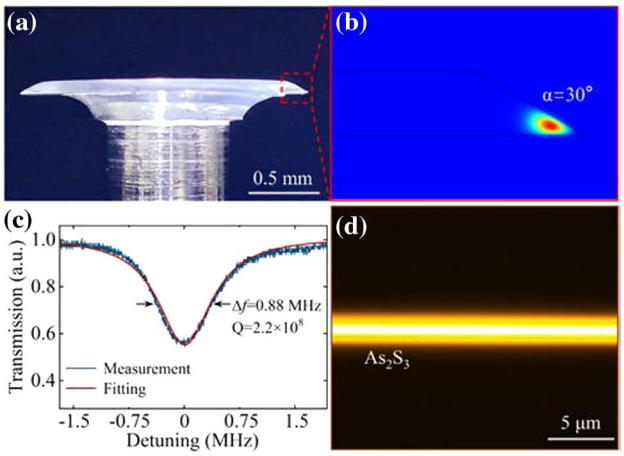

Fig. 1. (a) Image of the MgF_2 crystalline microresonator. (b) Calculated fundamental mode intensity profiles in resonators with 30° wedge angle at 4.78 μm. (c) Measured transmission spectrum (blue line) of the resonator and Lorentzian fit (red line) in the communication band. (d) Optical microscopic image of the As_2S_3 tapered fiber waist with a subwavelength diameter of ~1.5 μm.

3. NUMERICAL SIMULATION

As we all know, to generate an MIR Kerr frequency comb, engineering of the microresonator dispersion plays a critical role. The resonance frequency ω_μ of the modes can be Taylor-expanded around the center frequency ω_0 as [28]

$$\omega_\mu = \omega_0 + \mu D_1 + \frac{1}{2}\mu^2 D_2 + \frac{1}{6}\mu^3 D_3 + \cdots, \tag{1}$$

where μ is the mode number with respect to the pump mode ($\mu = 0$), $D_1/2\pi$ denotes the FSR, and D_2 is related to the GVD through the relation $D_2 = -c/n_0 D_1^2 \beta_2$, where c is the speed of light, n_0 is the refractive index, and D_3 represents the third-order dispersion. Figure 2(a) plots the simulated integrated dispersion curve $D_{\text{int}} = \omega_\mu - \omega_0 - \mu D_1$. It reveals that the resonator's anomalous dispersion $D_2/2\pi$ is ~0.67 MHz while higher-order terms are negligible. The nonlinear passive cavity dynamics in the MgF_2 microresonator and the corresponding Kerr frequency comb generation can be described by a normalized Lugiato–Lefever equation (LLE) [29]:

$$\frac{\partial \Psi}{\partial \tau} = -(1 + i\zeta_0)\Psi + i|\Psi|^2\Psi - \sum_{n=2}^{N}(-i)^{n+1}\frac{\beta_n}{n!}\frac{\partial^n \Psi}{\partial \theta^n} + f, \tag{2}$$

where $\Psi(\tau, \theta)$ is the slowly varying field amplitude, $\tau = \kappa t/2$ describes the normalized time, $\kappa = \kappa_0 + \kappa_{\text{ext}}$ is the cavity decay

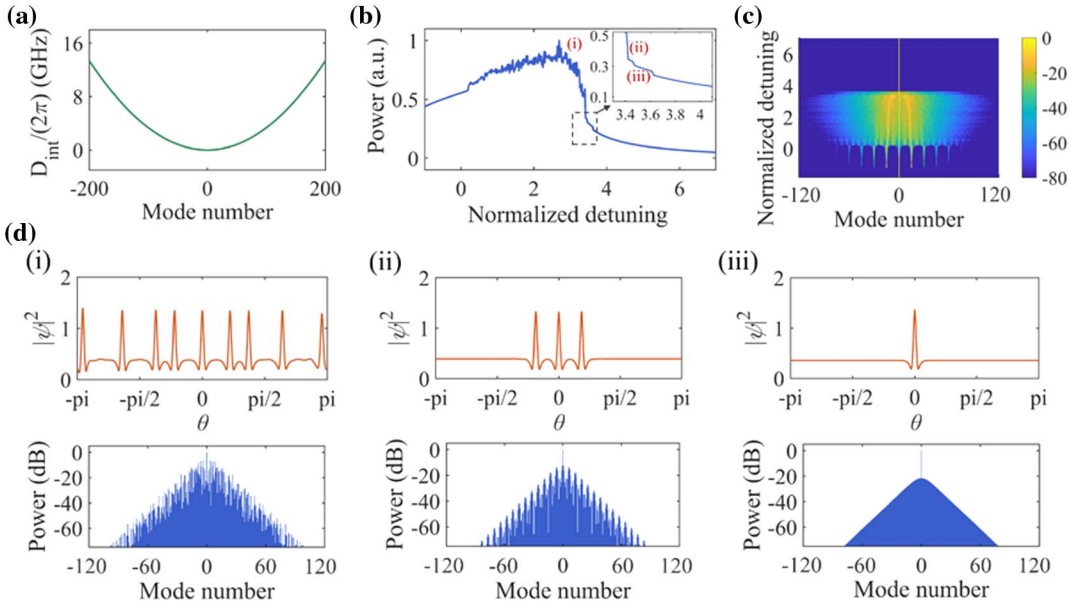

Fig. 2. (a) Integrated dispersion curve around the pump versus mode number μ. (b) Intracavity power as the pumping laser is tuned across a cavity resonance from the blue to red detuning. The inset shows the zoom-in for the dashed box. (c) Spectral envelope evolution corresponding to panel (b). (d) Temporal waveforms (orange) and optical spectra (blue) corresponding to the (i) MI, (ii) multi-soliton, and (iii) single-soliton states.

rate as the sum of intrinsic decay rate κ_0 and coupling rate to the waveguide κ_{ext}, $\zeta_0 = 2(\omega_0 - \omega_p)/\kappa$ denotes the normalized detuning as the pump laser ω_p from the cold resonance frequency ω_0, β_n represents the nth order dispersion term, $\theta \in [-\pi, \pi]$ is the azimuthal angle along the rim of the resonator, $f = \sqrt{8g\eta P_{\text{in}}/(\kappa^2\hbar\omega_0)}$ is the external pump related to the pump power P_{in}, $\eta = \kappa_{\text{ext}}/\kappa$ is the coupling efficiency, $g = \hbar\omega_p^2 c n_2/(n_0^2 V_{\text{eff}})$ describes the nonlinear gain coefficient, in which $\hbar$ is the Planck constant, ω_p is the pump frequency, c is the speed of light, $V_{\text{eff}} = A_{\text{eff}} L$ is the effective cavity nonlinear volume with the effective mode area A_{eff} and circumference of the cavity L, and n_0 and n_2 denote the refractive index and nonlinear refractive index, respectively.

To understand and observe the detailed process associated with soliton formation in a MgF_2 microresonator, numerical simulations are carried out based on the LLE. Similar to the numerical analysis in the near-infrared [29,30], the thermal effect is also neglected. In practice, it will lead to the resonance shift and, thus, affect the effective detuning. This could be solved by choosing an appropriate wavelength tuning speed of the pump laser such that the resonator could reach the soliton state in a thermal equilibrium. Figure 2(b) depicts the variation of the intracavity average power versus the pump-resonance detuning at pump power $P_{\text{in}} = 300$ mW, which has terraced soliton solution states [see the inset of Fig. 2(b)]. As the pump wavelength increases from the blue-detuned side to the effectively red-detuned side, the microcomb transitions from the MI state to multi-soliton state and eventually to the steady single-soliton state. It can be obviously found that the intracavity power has a large drop during the evolution of the MI state to the soliton regime in the cavity. The spectrum evolution of the cavity field versus pump-resonance detuning is also observed in Fig. 2(c), which shows the generation of the Kerr frequency comb. With the pump laser tuning across a cavity resonance from the blue to red detuning, MI and chaotic states of the intracavity field are first observed, where the temporal and spectral distribution is erratic [region (i) of Fig. 2(d)]. The chaotic region is clearly indicated by the large oscillation of the energy. Moreover, multi-soliton states could also be excited in a small range of ζ_0 (e.g., 3.421–3.456), where the intracavity fields become relatively stable [region (ii) of Fig. 2(d)]. Finally, the sech^2-shape spectrum can be obtained by further

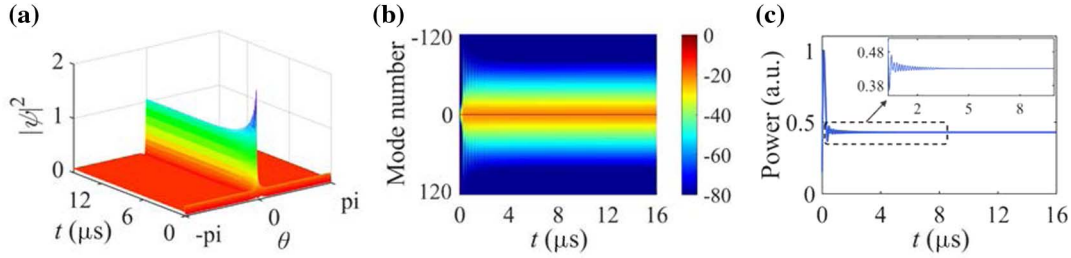

Fig. 3. (a) Temporal and (b) spectral evolution of the single soliton formation. (c) Evolution of intracavity average power plotted versus time. The inset shows the zoom-in for the dashed square.

increasing ζ_0 (e.g., >3.473), indicating that the comb reaches the steady single-soliton state [region (iii) of Fig. 2(d)].

To further reveal single-soliton-based frequency comb generation dynamics in the MgF_2 resonator, the temporal and spectral evolutions of the cavity field are investigated with the normalized detuning $\zeta_0 \sim 3.56$ at $P_{in} = 300$ mW, as shown in Figs. 3(a) and (b), respectively. Additionally, the corresponding variations of time-dependent intracavity power are given in Fig. 3(c). Note that the intracavity average power will undergo a relaxation oscillation in the initial several microseconds [inset of Fig. 3(c)], then increase slowly in the long thermal stabilization process, and eventually converge to a constant power. This indicates that a stabilized microresonator-based MIR OFC can be realized with appropriate pump-resonance detuning and pump power [30].

4. EXPERIMENTAL DEMONSTRATION

Schematic illustration of the experimental setup for MIR OFC generation using a crystalline MgF_2 microresonator is shown in Fig. 4. A continuous-wave pump light is generated from a tunable QCL with a spectral linewidth less than 3.5 MHz, as shown in the inset of Fig. 4. The input light is polarization-adjusted by a half-wave plate and focused by an aspheric lens onto one end face of ChG tapered fiber, which is stably controlled by fixing it with a glass slide. The evanescent coupling is achieved by adjusting the distance between the MgF_2 crystalline microresonator and the ChG tapered fiber. Furthermore, the phase matching can be finely tuned by translating the microresonator along the taper of the fiber relative to the waist. The signal output from the tapered fiber is collimated by another aspheric lens and is split by a beam splitter. The reflected light is recorded by a photodetector and an oscilloscope to monitor the cavity resonance. The transmitted light is injected into a Fourier transform infrared spectrometer (Bruker VERTEX 80) for the spectrum analysis.

The QCL module is operated at 4.78 μm as illustrated in Fig. 5(a) (black line), and its tunable wavelength range is approximately 10 nm by adjusting the working temperature. The MIR frequency comb is generated by pumping a cavity resonance of a MgF_2 microresonator. From the theoretical simulation, we notice that the pump laser detuning is a critical parameter in Kerr OFC generation. To search the effective pump-resonance detuning, the pump laser is scanned with decreasing optical frequency ω_p over an FSR. A sudden growth of the power floor can be observed on the oscilloscope, and the parametric frequency conversion will occur when the pump frequency is tuned to one of the resonances of the microresonator. Figures 5(a) and (b) show the output spectra in the MgF_2 resonators with different sizes via tuning the pump wavelength at a fixed pump power of approximately 150 mW (estimated as ~70 mW inside the tapered fiber), which is processed by the min-max normalization method [31]. While continuously increasing the pump-resonance detuning, more and more new frequency components are generated by the cascade FWM [29]. This phenomenon coincides with the transition from the blue-detuned regime to the red-detuned regime of Kerr frequency combs [28]. The broadband MIR optical parametric oscillation with evenly spaced modes is also obtained in the MgF_2 resonators with different diameters at a proper pump detuning, as illustrated in Fig. 5(c). The spectral distance of ~1.59 THz is acquired in a ~2 mm diameter MgF_2 resonator, while it is ~0.81 THz in the ~9 mm diameter MgF_2 resonator. This mainly results from the different whispering-gallery modes excited by pumping different radial modes in the microresonator [32]. Furthermore, the FSR and dispersion vary with the structure parameters and will also lead to different mode spacing in microresonators with different sizes [33,34].

Next, we investigate the generation of MIR frequency comb by optimizing pump-resonance detuning and pump power in a MgF_2 resonator with a diameter of ~2 mm. Figure 6(a) shows the parametric oscillation spectrum operated at approximately 200 mW, where one can observe the onset of MIR frequency comb generation. Moreover, when the input pump power is about 240 mW, the spectral components of the comb are obviously broadened and increased based on the cascaded FWM process, as presented in Fig. 6(b). This can be interpreted that the broadband phase matching could be satisfied through tuning the pump power and pump-resonance detuning, giving rise to the increase of the parametric gain bandwidth [35]. Further increasing the pump power to ~280 mW, the comb lines fill ulteriorly the spectrum, and an ultra-broadband MI state MIR frequency comb over an octave from 3380 nm to 7760 nm is obtained, as elucidated in Fig. 6(c). Indeed, limited by the

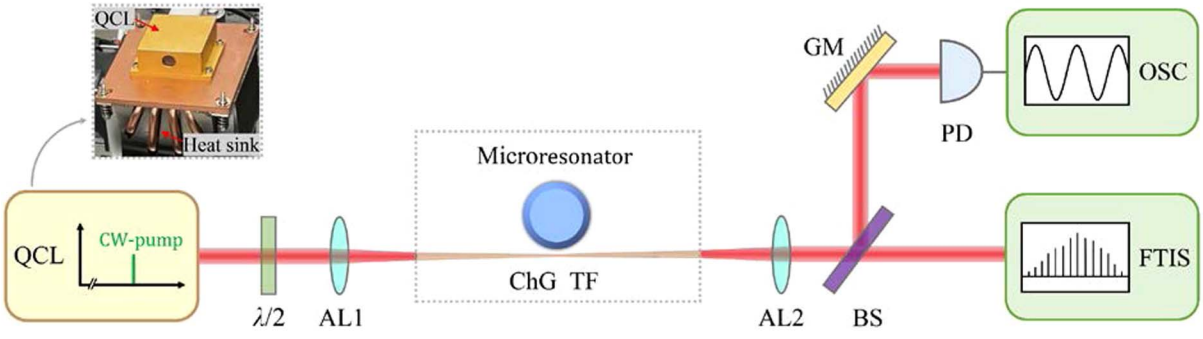

Fig. 4. Experimental setup for the generation of MIR OFCs in the MgF_2 resonator. QCL, quantum cascade laser (inset, photograph of QCL module); AL, aspheric lens; ChG TF, As_2S_3 tapered fiber; BS, beam splitter; PD, photodetector; OSC, oscilloscope; GM, gold mirror; FTIS, Fourier transform infrared spectrometer.

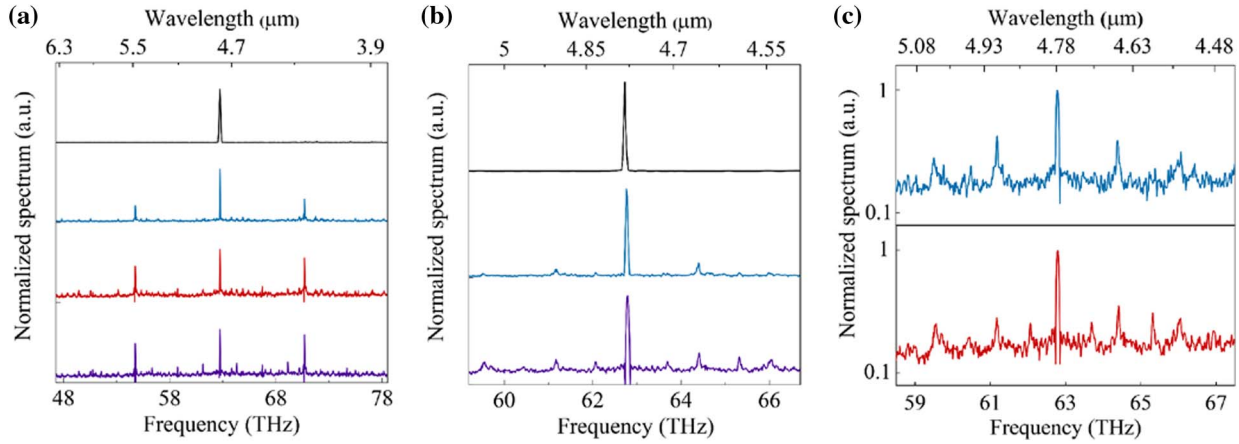

Fig. 5. MIR frequency comb spectrum with different pump-resonance detuning in the MgF_2 resonators of (a) ~2 mm diameter and (b) ~9 mm diameter, and the pump QCL operated at 4.78 μm (black line). (c) MIR frequency comb spectrum with evenly spaced modes in MgF_2 resonators with diameters of ~2 mm (blue line) and ~9 mm (red line).

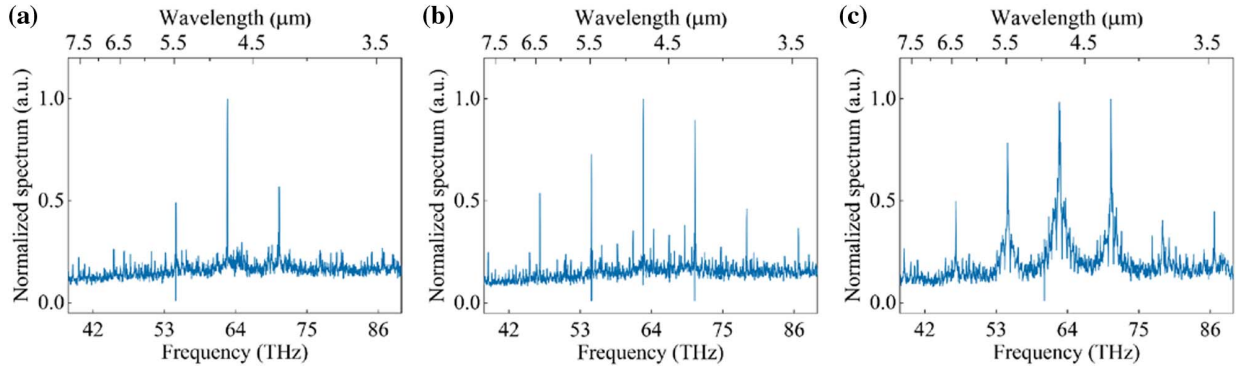

Fig. 6. MIR frequency comb spanning from 3380 nm to 7760 nm. Spectrum generated by a ~2 mm diameter MgF_2 resonator under pump power of about (a) 200 mW, (b) 240 mW, and (c) 280 mW.

performance of the QCL and MgF_2 microresonator, the generated frequency comb is in the MI states, similar to the spectrum in region (i) of Fig. 2(d). Compared with the MIR OFC reported by Refs. [18,19,36–38], our results demonstrate the potential of the MgF_2 crystalline resonator in octave-spanning OFC generation, which makes the f-$2f$ self-referencing method feasible. Greater bandwidth is also very important for practical applications. It is anticipated that the fully stabilized MIR soliton frequency comb generation with low-phase-noise based on the MgF_2 crystalline microresonator and QCL is feasible, triggered by the progress of the fabrication technique for high Q factor crystalline microresonators or high-power laser sources in the future.

5. SUMMARY

In conclusion, we report the broadband MIR OFC generation in a MgF_2 crystalline microresonator pumped by a QCL. The MgF_2 resonator with a high Q factor is obtained by optimizing the resonator's geometry parameters. A steep transition from the MI to stable soliton state via the pump frequency tuning approach is observed in numerical simulation. The MI state MIR OFC ranging from 3380 nm to 7760 nm is generated experimentally based on the cascaded FWM in the resonator. This work would then represent an essential building block paving the road for MIR soliton frequency combs generated in microresonators.

Funding. National Natural Science Foundation of China (61635013); Natural Science Basic Research Program of Shaanxi Province (2022JC-43).

Acknowledgment. The authors thank Prof. Haitao Guo of Xi'an Institute of Optics and Precision Mechanics of CAS for the support of mid-infrared fibers, Prof. Fengqi Liu of Institute of Semiconductors of CAS for the support of QCLs, and Zhejiang University and Peking University for the support of tapered fiber fabrication.

Disclosures. The authors declare no conflicts of interest.

Data Availability. Data underlying the results presented in this paper are not publicly available at this time but may be obtained from the authors upon reasonable request.

REFERENCES

1. S. Kim, K. Han, C. Wang, J. A. Jaramillo-Villegas, X. Xue, C. Bao, Y. Xuan, D. E. Leaird, A. M. Weiner, and M. Qi, "Dispersion engineering and frequency comb generation in thin silicon nitride concentric microresonators," Nat. Commun. **8**, 372 (2017).
2. S. Wan, R. Niu, Z.-Y. Wang, J.-L. Peng, M. Li, J. Li, G.-C. Guo, C.-L. Zou, and C.-H. Dong, "Frequency stabilization and tuning of breathing solitons in Si_3N_4 microresonators," Photon. Res. **8**, 1342–1349 (2020).
3. H.-J. Chen, Q.-X. Ji, H. Wang, Q.-F. Yang, Q.-T. Cao, Q. Gong, X. Yi, and Y.-F. Xiao, "Chaos-assisted two-octave-spanning microcombs," Nat. Commun. **11**, 2336 (2020).
4. F.-X. Wang, W. Wang, R. Niu, X. Wang, C.-L. Zou, C.-H. Dong, B. E. Little, S. T. Chu, H. Liu, P. Hao, S. Liu, S. Wang, Z.-Q. Yin, D.-Y. He, W. Zhang, W. Zhao, Z.-F. Han, G.-C. Guo, and W. Chen, "Quantum key distribution with on-chip dissipative Kerr soliton," Laser Photon. Rev. **14**, 1900190 (2020).
5. A. W. Bruch, X. Liu, Z. Gong, J. B. Surya, M. Li, C.-L. Zou, and H. X. Tang, "Pockels soliton microcomb," Nat. Photonics **15**, 21–27 (2021).
6. K. Luke, Y. Okawachi, M. R. E. Lamont, A. L. Gaeta, and M. Lipson, "Broadband mid-infrared frequency comb generation in a Si_3N_4 microresonator," Opt. Lett. **40**, 4823–4826 (2015).
7. M. Seidel, X. Xiao, A. H. Syed, G. Arisholm, A. Hartung, T. Z. Kevin, G. S. Peter, F. Habel, M. Trubetskov, V. Pervak, O. Pronin, and F. Krausz, "Multi-watt, multi-octave, mid-infrared femtosecond source," Sci. Adv. **4**, eaaq1526 (2018).
8. A. Schliesser, N. Picqué, and T. W. Hänsch, "Mid-infrared frequency combs," Nat. Photonics **6**, 440–449 (2012).
9. H. Lin, Z. Luo, T. Gu, L. C. Kimerling, K. Wada, A. Agarwal, and J. Hu, "Mid-infrared integrated photonics on silicon: a perspective," Nanophotonics **7**, 393–420 (2018).
10. M. Yu, Y. Okawachi, A. G. Griffith, N. Picqué, M. Lipson, and A. L. Gaeta, "Silicon-chip-based mid-infrared dual-comb spectroscopy," Nat. Commun. **9**, 1869 (2018).
11. G. Ycas, F. R. Giorgetta, E. Baumann, I. Coddington, D. Herman, S. A. Diddams, and N. R. Newbury, "High-coherence mid-infrared dual-comb spectroscopy spanning 2.6 to 5.2 μm," Nat. Photonics **12**, 202–208 (2018).
12. B. Kuyken, T. Ideguchi, S. Holzner, M. Yan, T. W. Hänsch, J. Van Campenhout, P. Verheyen, S. Coen, F. Leo, R. Baets, G. Roelkens, and N. Picqué, "An octave-spanning mid-infrared frequency comb generated in a silicon nanophotonic wire waveguide," Nat. Commun. **6**, 6310 (2015).
13. A. L. Gaeta, M. Lipson, and T. J. Kippenberg, "Photonic-chip-based frequency combs," Nat. Photonics **13**, 158–169 (2019).
14. A. Pasquazi, M. Peccianti, L. Razzari, D. J. Moss, S. Coen, M. Erkintalo, Y. K. Chembo, T. Hansson, S. Wabnitz, P. Del'Haye, X. Xue, A. M. Weiner, and R. Morandotti, "Micro-combs: a novel generation of optical sources," Phys. Rep. **729**, 1–81 (2018).
15. C. Xiang, J. Liu, J. Guo, L. Chang, N. W. Rui, W. Weng, J. Peters, W. Xie, Z. Zhang, J. Riemensberger, J. Selvidge, J. K. Tobias, and E. B. John, "Laser soliton microcombs heterogeneously integrated on silicon," Science **373**, 99–103 (2021).
16. H. Guo, C. Herkommer, A. Billat, D. Grassani, C. Zhang, M. H. P. Pfeiffer, W. Weng, C.-S. Brès, and T. J. Kippenberg, "Mid-infrared frequency comb via coherent dispersive wave generation in silicon nitride nanophotonic waveguides," Nat. Photonics **12**, 330–335 (2018).
17. M. Yu, Y. Okawachi, A. G. Griffith, M. Lipson, and A. L. Gaeta, "Mode-locked mid-infrared frequency combs in a silicon microresonator," Optica **3**, 854–860 (2016).
18. A. A. Savchenkov, V. S. Ilchenko, F. Di Teodoro, P. M. Belden, W. T. Lotshaw, A. B. Matsko, and L. Maleki, "Generation of Kerr combs centered at 4.5 μm in crystalline microresonators pumped with quantum-cascade lasers," Opt. Lett. **40**, 3468–3471 (2015).
19. C. Y. Wang, T. Herr, P. Del'Haye, A. Schliesser, J. Hofer, R. Holzwarth, T. W. Hänsch, N. Picqué, and T. J. Kippenberg, "Mid-infrared optical frequency combs at 2.5 μm based on crystalline microresonators," Nat. Commun. **4**, 1345 (2013).
20. I. S. Grudinin, K. Mansour, and N. Yu, "Properties of fluoride microresonators for mid-IR applications," Opt. Lett. **41**, 2378–2381 (2016).
21. M. Razeghi, Q. Y. Lu, N. Bandyopadhyay, W. Zhou, D. Heydari, Y. Bai, and S. Slivken, "Quantum cascade lasers: from tool to product," Opt. Express **23**, 8462–8475 (2015).
22. L. Tombez, S. Schilt, D. Hofstetter, and T. Südmeyer, "Active linewidth-narrowing of a mid-infrared quantum cascade laser without optical reference," Opt. Lett. **38**, 5079–5082 (2013).
23. M. Wang, Y. Yang, L. Meng, X. Jin, Y. Dong, L. Zhang, W. Xu, and K. Wang, "Fabrication and packaging for high-Q CaF_2 crystalline resonators with modal modification," Chin. Opt. Lett. **17**, 111401 (2019).
24. B. Bendow, H. G. Lipson, and S. S. Mitra, "Multiphonon infrared absorption in highly transparent MgF_2," Phys. Rev. B **20**, 1747–1749 (1979).
25. D. D. Hudson, S. Antipov, L. Li, I. Alamgir, T. Hu, M. E. Amraoui, Y. Messaddeq, M. Rochette, S. D. Jackson, and A. Fuerbach, "Toward all-fiber supercontinuum spanning the mid-infrared," Optica **4**, 1163–1166 (2017).
26. G. Li, X. Peng, S. Dai, Y. Wang, M. Xie, L. Yang, C. Yang, W. Wei, and P. Zhang, "Highly coherent 1.5–8.3 μm broadband supercontinuum generation in tapered As–S chalcogenide fibers," J. Lightwave Technol. **37**, 1847–1852 (2019).
27. Y. Xie, D. Cai, H. Wu, J. Pan, N. Zhou, C. Xin, S. Yu, P. Wang, X. Jiang, J. Qiu, X. Guo, and L. Tong, "Mid-infrared chalcogenide microfiber knot resonators," Photon. Res. **8**, 616–621 (2020).
28. J. K. Tobias, L. G. Alexander, M. Lipson, and L. G. Michael, "Dissipative Kerr solitons in optical microresonators," Science **361**, eaan8083 (2018).
29. T. Herr, V. Brasch, J. D. Jost, C. Y. Wang, N. M. Kondratiev, M. L. Gorodetsky, and T. J. Kippenberg, "Temporal solitons in optical microresonators," Nat. Photonics **8**, 145–152 (2014).
30. H. Guo, M. Karpov, E. Lucas, A. Kordts, M. H. P. Pfeiffer, V. Brasch, G. Lihachev, V. E. Lobanov, M. L. Gorodetsky, and T. J. Kippenberg, "Universal dynamics and deterministic switching of dissipative Kerr solitons in optical microresonators," Nat. Phys. **13**, 94–102 (2017).
31. D. K. Agustika, I. Mercuriani, C. W. Purnomo, S. Hartono, K. Triyana, D. D. Iliescu, and M. S. Leeson, "Fourier transform infrared spectrum pre-processing technique selection for detecting PYLCV-infected chilli plants," Spectrochim. Acta A **278**, 121339 (2022).
32. G. Lin and Y. K. Chembo, "On the dispersion management of fluorite whispering-gallery mode resonators for Kerr optical frequency comb generation in the telecom and mid-infrared range," Opt. Express **23**, 1594–1604 (2015).
33. T. Herr, K. Hartinger, J. Riemensberger, C. Y. Wang, E. Gavartin, R. Holzwarth, M. L. Gorodetsky, and T. J. Kippenberg, "Universal formation dynamics and noise of Kerr-frequency combs in microresonators," Nat. Photonics **6**, 480–487 (2012).
34. B. Zhang, P. Zeng, Z. Yang, D. Xia, J. Zhao, Y. Sun, Y. Huang, J. Song, J. Pan, H. Cheng, D. Choi, and Z. Li, "On-chip chalcogenide microresonators with low-threshold parametric oscillation," Photon. Res. **9**, 1272–1279 (2021).
35. N. L. B. Sayson, T. Bi, V. Ng, H. Pham, L. S. Trainor, H. G. L. Schwefel, S. Coen, M. Erkintalo, and S. G. Murdoch, "Octave-spanning tunable parametric oscillation in crystalline Kerr microresonators," Nat. Photonics **13**, 701–706 (2019).
36. C. Lecaplain, C. Javarzac-Galy, E. Lucas, J. D. Jost, and T. J. Kippenberg, "Quantum cascade laser Kerr frequency comb," in *European Conference on Lasers and Electro-Optics-European Quantum Electronics Conference* (2015), paper CB_10_16.
37. C. Lecaplain, C. Javarzac-Galy, E. Lucas, J. D. Jost, and T. J. Kippenberg, "Quantum cascade laser Kerr frequency comb generation," in *Conference on Lasers and Electro-Optics (CLEO)* (2015), paper SW4F.2.
38. C. Lecaplain, C. Javarzac-Galy, E. Lucas, J. D. Jost, and T. J. Kippenberg, "Quantum cascade laser Kerr frequency comb," in *Frontiers in Optics* (2015), paper FTu3E.2.